

An Online Self-Correction Method to Improve Accuracy of Split-Core Current Transformer in Low-Voltage Distribution Networks

Jie Teng^a, Shaorong Wang^{a,*}, Lin Jiang^b, Wei Xie^c, Chen Fang^d and Shu Liu^d

^aSchool of Electrical and Electronic Engineering, Huazhong University of Science and Technology, Wuhan, 430074, China

^bDepartment of Electrical Engineering and Electronics, University of Liverpool, Liverpool, L69 3GJ, UK

^cState Grid Shanghai Municipal Electric Power Company

^dState Grid Shanghai Electric Power Research Institute

ARTICLE INFO

Keywords:

split-core current transformer
varying magnetizing error
auxiliary winding loop
self-correction algorithm
low-cost implementation

ABSTRACT

Split-core current transformer (CT) has been widely used in low-voltage distribution networks due to the merit of live-line installation. However, as the air gaps of the iron core exist, there is a possibly varying magnetizing error, which will severely degrade the accuracy of split-core CT, caused by manual installation deviation, vibration, and temperature variation in field operation. To tackle this issue, this paper proposes an online self-correction method to improve the measurement accuracy of split-core CT. The proposed method contains 1) an auxiliary winding loop (AWL) added to the split-core CT, to temporarily and intermittently operate in on/off modes; and 2) a self-correction algorithm (SCA) based on the operation of the AWL, to online determine the varying errors and then to give corrected measurement results. Moreover, a low-cost solution for embedding the proposed method in multiple split-core CTs in low-voltage distribution network is provided via series-connecting the AWLs. For validation, a prototype embedded with the proposed method is implemented, and is tested versus different applied primary currents and burdens. The test results exhibit that the proposed method effectively improves the measurement accuracy to a high class (0.2). Also, the proposed method's robustness to varying gap lengths and temperatures is verified. Notably, even under the extreme condition with a 0.520 mm gap, the measurement errors are reduced from the inherent values up to 30.9% and 648 mrad to a satisfactory range below 0.195% and 0.295 mrad, respectively.

1. Introduction

The core construction of split-core current transformer (CT) can hinge open or totally separate into two halves [1, 2]. This special arrangement leads to the convenience of live-line installation [3], and thus contributes to the wide usage of the split-core CT in low-voltage distribution networks monitoring [4]. However, as its magnetic circuit is interrupted by the air gaps, a relatively large unbalanced ampere-turn between the primary and secondary is introduced and in turn results in a higher-than-normal magnetizing error degrading the accuracy of the split-core CT [5–7]. Split-core CTs usually have an accuracy class of at most 0.5 (and 1 and 3), while solid CTs can be more accurate with a class of 0.2 and 0.2S.

The accuracy of split-core CTs can be improved via material selection or structure design at the design stage [8]. For instance, the appropriate cut cores (e.g., oval and toroidal) and the advanced materials (e.g., polycrystalline and nanocrystalline) with extraordinary magnetic properties can achieve a small magnetizing error under the conditions contenting the design requirements [9]. However, the reassembly of the core halves is critical since it is hard to perfectly ensure the alignment of two core halves and the sufficiently small gap length (smaller than 15 μm , as demanded in [10]). There is

also some uncertainty in the repeatability of manual performance from installation to installation. Then this uncertainty will impose a change on the magnetizing error and offset the advantages of the magnetic properties. Another way proposed in [11] uses a feedback circuit to actively compensate the magnetizing error, where a tertiary winding and a tertiary core are employed. The effect of compensation heavily relies on the high permeability of the tertiary core, which is further compounded by the aforementioned installation uncertainty of the split-core CT. In view of this deficiency, some improvement for the compensation can be obtained via utilizing a multi-stage split-core CT with nested or side-by-side cores [12, 13]. These feedback compensating methods can be effective against the installation uncertainty, but they will considerably increase the complexity and cost of the split-core CT. Besides, the error of the split-core CT can be digitally compensated depending on the magnetization curve [14]. The requirement for the secondary impedances makes this method impractical, since these parameters can change due to temperature variation.

Alternatively, a common way to improve the accuracy of split-core CT under laboratory conditions is calibration [15]. The calibration for the split-core CT (even all types of CT) is usually carried out with the comparative method, aimed at determining the magnetizing error, i.e., the ratio error and the phase displacement. The comparative method compares the secondary current of the CT under test with that of the standard instrument (such as the calibrated CT, the calibrated Rogowski coil, or the current comparator) applied with the same primary current [16]. The authors of [17] utilize a

*Corresponding author

tengjie@hust.edu.cn (J. Teng); wsrwy96@vip.sina.com (S. Wang);
e-mail: ljiang@liv.ac.uk (L. Jiang); SAMEDSON@HOTMAIL.COM (W. Xie);
fangc02@139.com (C. Fang); liuxshu2012@163.com (S. Liu)

ORCID(s): 0000-0001-6702-3571 (J. Teng); 0000-0001-6239-2845 (S. Wang); 0000-0001-6531-2791 (L. Jiang); 0000-0001-6331-6860 (W. Xie); 0000-0001-8877-0111 (C. Fang); 0000-0002-3035-2213 (S. Liu)

step-down transformer with multiple primary and secondary windings as the standard CT, which can all be connected in series or parallel, to provide higher ratio flexibility of calibration. Instead of respectively measuring the secondary currents of the CT under test and the standard CT, a differential circuit is provided in [18] to measure the difference between the two secondary currents directly. Similarly, the difference between the secondary currents can be obtained via an additional winding to detect the magnetic flux, when the secondary windings of the CT under test and the standard CT are connected in subtractive series [19]. Finally, the performances of those calibration studies have been verified by tests under different applied primary currents (with different magnitudes and frequencies) and different burdens [20, 21]. Some of them have been successfully applied in industry [22, 23]. However, these calibration methods cannot effectively improve the accuracy of the split-core CT in the field. At first, the deviation of manual installation will inevitably change the gap length after installation, which will generate a magnetizing error different from that determined by the calibration in the laboratory. Moreover, the gap length might vary slowly during the long term in field operation, due to environmental factors such as vibration and temperature variation. In fact, these variations of the magnetizing error cannot be effectively addressed by the traditional calibration methods to ensure the accuracy of the split-core CT.

In summary, the main challenges for improving the accuracy of the split-core CT are: 1) manual installation causes an uncertain magnetizing error; 2) the error changes due to environmental variations in field are hard to track; and 3) as split-core CTs are massively installed for monitoring in distribution networks, the cost should be as low as possible. To resolve these challenges, this paper proposes an online self-correction method (OSC), including two key parts, i.e., an auxiliary winding loop (AWL) configured in hardware and a self-correction algorithm (SCA) embedded in the digital signal processing unit. The AWL temporarily operates in on/off modes so as to intermittently inject an auxiliary current to the split-core CT. Then the SCA acquires the response of the secondary current once in a while, to determine the CT error. Finally, the determined error is used to correct the measurement results of the split-core CT in the long term. The main contributions of this paper are listed as: 1) this paper provides a unique solution without interruption of measurement to significantly improve the accuracy of the split-core CT, which can be implemented with a low cost for multiple split-core CTs in low-voltage distribution network; 2) the proposed method is robust to the varying errors caused by manual installation deviation, vibration, and temperature variation in field operation. Moreover, a prototype implementation of the OSC and the experimental tests are presented to verify the effectiveness.

The rest of this paper is organized as follows. Section 2 introduces the general design of the OSC. In section 3, the principle of operation is given in detail. The implementation of a prototype and experimental tests are shown in section 4. Section 5 draws the conclusion.

2. General Design of Split-core CT with OSC

The general design of the OSC is given in Fig. 1. In the conventional CT measurement system, i_p , i_s , and N_s are the primary current, the secondary current, and the turn ratio of the split-core CT, respectively. The magnitude and the initial phase of i_s are correspondingly denoted as A_s and φ_s , usually given by the calculation program. And the measurement results $N_s A_s$ and φ_s without correction are used to represent the magnitude and the initial phase of i_p , with a ratio error ε and a phase displacement δ compared with the real values of i_p , i.e., magnitude A_p and initial phase φ_p . The OSC includes two key parts, i.e., an auxiliary winding loop (AWL), and a self-correction algorithm (SCA). The AWL is configured in hardware, to temporarily and intermittently inject an auxiliary current i_a into the split-core CT. Then the SCA, running in the digital signal processing system, acquires i_a and the response of i_s once in a while to calculate ε and δ of the split-core CT (represented in the blue dashed box). Finally, ε and δ are utilized to obtain the corrected values of i_p as $A_p = (1 + \varepsilon)N_s A_s$ and $\varphi_p = \varphi_s + \delta$ (the green dashed box), respectively.

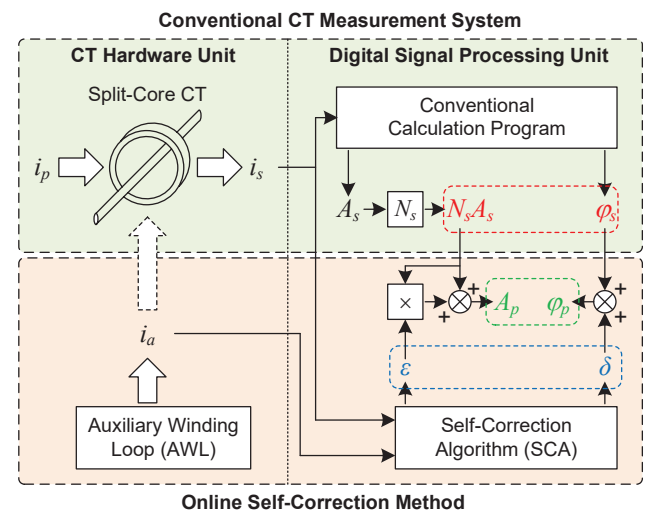


Figure 1: General design of OSC

More explicitly, the OSC can be embedded in a split-core CT, as shown in Fig. 2. The AWL is comprised of an auxiliary winding, an auxiliary current source, an electronic switch, a varistor R_V , and a current shunt resistor R_2 . The auxiliary winding is uniformly distributed along one half of the split core. The current signal i_a provided by the auxiliary current source is supposed to have the same power frequency as that of i_p . The electronic switch controls the AWL operating in off/on modes. At the off mode, the auxiliary current source is switched out of the AWL and does not affect i_s . At the on mode, i_s will additionally response to i_a . To get rid of the over-voltage produced by the open-circuit AWL in the off mode, R_V is deployed. Meanwhile, since the secondary winding circuit of the split-core CT is always closed, unexpected over-voltage will not occur. The DSP unit (included in the blue dashed box) collects i_s and i_a via the current shunts (R_1 and R_2) and analog-to-digital conversion cir-

cuit (ADC). Also, the DSP unit generates the control signal $g = 0$ or 1 for the electronic switch in a specially designed timing. Moreover, the OSC runs only when self-correction is required. Thus in normal measurement, the OSC is disabled and the electronic switch is always off. The design of the above components in detail will be presented in Section 4.

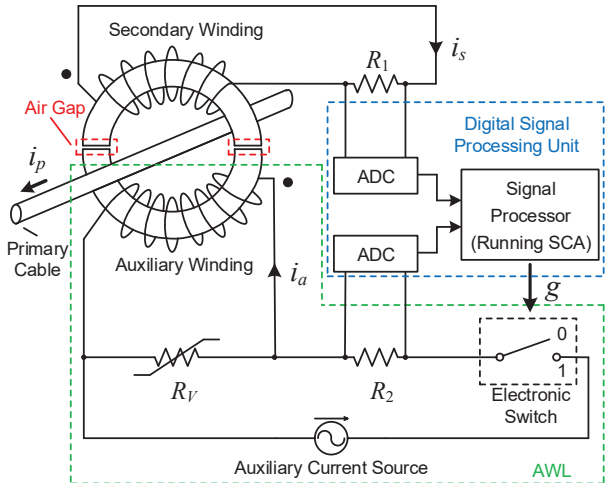


Figure 2: Schematic diagram of split-core CT embedded with OSC

Furthermore, in low-voltage distribution network, the solution for embedding the OSC in multiple split-core CTs on multiple lines is provided as Fig. 3. By series-connecting the AWLs of all the split-core CTs, one set of the auxiliary current source, electronic switch, sampling channel, and DSP unit are shared. Thus additional cost to implement the proposed method will be relatively low.

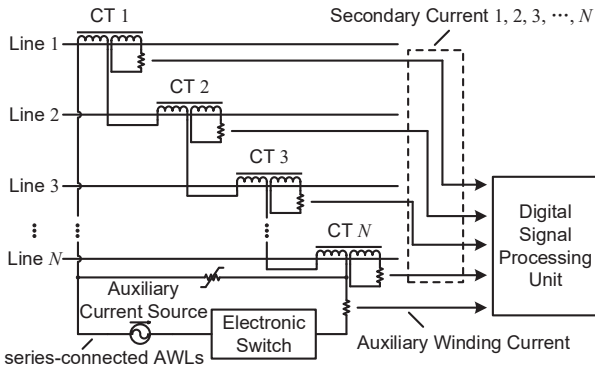


Figure 3: Diagram of OSC for multiple split-core CTs

2.1. Equivalent Circuit

The operation principle of the OSC is derived from the equivalent circuit model of split-core CT. A typical s -domain equivalent circuit of a single split-core CT embedded with the OSC is shown in Fig. 4, where N_a is the turn number of the auxiliary winding. The parameters of the equivalent circuit are all referred to the primary side. The resistors R_p , R_s , and R_a are the wire resistances of the primary, secondary and auxiliary windings, respectively. L_p , L_s , and L_a denote the leakage inductances to describe the leakage fluxes of the windings. Besides, $L_m // R_m$ is the magnetizing branch, and

I_m represents the magnetizing current. Wherein, L_m is used to describe the magnetization characteristics of the core, i.e., the flux-current curve, depending on the material and shape of the core. As the magnetization characteristics of the core are in fact non-linear, e.g., core saturation, the value of L_m varies with the magnitude and frequency of the magnetizing current, and can be influenced by other harmonics. And L_m is relevant to the length of the air gap. R_m represents the frequency-dependent resistance of the core loss. The equivalent circuit indicates that ϵ and δ tracked by the OSC are contributed by two categories of components: 1) burden error related to the wire resistances and the leakage inductances, which will change due to variations of temperature and burden R_1 ; and 2) magnetizing error owing to the magnetizing branch. Generally, this error of split-core CT is larger than that of solid CT, since the existence of air gaps decreases the impedance of magnetizing branch. And the change of gap length will result in a varying magnetizing error.

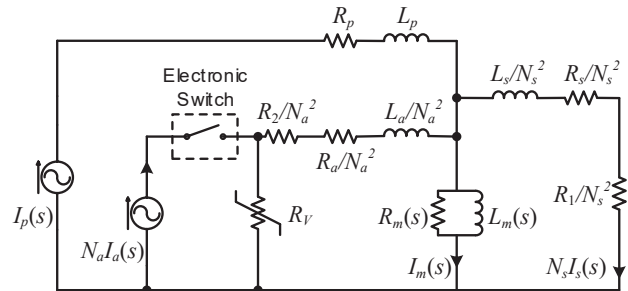


Figure 4: Equivalent circuit of the split-core CT embedded with OSC

Based on the equivalent circuit at off/on modes, the magnetomotive force (mmf) balance equation always works as below, no matter how the above parameters change:

$$I_p^{(k)}(s) - I_m^{(k)}(s) = N_s I_s^{(k)}(s) - N_a I_a^{(k)}(s) \quad (1)$$

where $k = 0$ or 1 represents the off/on mode of the AWL. If the primary current is a distorted one composed of the fundamental and harmonics, each frequency component is in compliance with (1). In follows, only the fundamentals are discussed for simplicity. Thus (1) in time domain is utilized as the basis of the calculation by the OSC as:

$$\begin{aligned} & \sqrt{2}A_p \sin(2\pi ft + \varphi_p^{(k)}) - \sqrt{2}A_m^{(k)} \sin(2\pi ft + \varphi_m^{(k)}) \\ &= \sqrt{2}N_s A_s^{(k)} \sin(2\pi ft + \varphi_s^{(k)}) - \sqrt{2}N_a A_a^{(k)} \sin(2\pi ft + \varphi_a^{(k)}) \end{aligned} \quad (2)$$

where A_p , $A_m^{(k)}$, $A_s^{(k)}$ and $A_a^{(k)}$ are the magnitudes (RMS) of the fundamentals of $i_p^{(k)}$, $i_m^{(k)}$, $i_s^{(k)}$ and $i_a^{(k)}$, respectively; $\varphi_p^{(k)}$, $\varphi_m^{(k)}$, $\varphi_s^{(k)}$ and $\varphi_a^{(k)}$ are the phases of the fundamentals, respectively. f represents the power frequency. Specifically, when $k = 0$, $A_a^{(k)}$ equals 0.

If the magnitude of i_a is sufficiently small, within a short enough correction cycle, it can be assumed that: 1) A_p and f are unchanged; and 2) R_p , L_p , R_s , L_s , R_1 , R_a , L_a , R_2 , R_m , and L_m are constants. Based on the above assumptions, the

magnitude ratio and phase difference of $i_s^{(k)}$ and $i_m^{(k)}$ always satisfy the equations as below, respectively:

$$\frac{A_m^{(0)}}{A_s^{(0)}} = \frac{A_m^{(1)}}{A_s^{(1)}} \quad (3)$$

$$\varphi_m^{(0)} - \varphi_s^{(0)} = \varphi_m^{(1)} - \varphi_s^{(1)} \quad (4)$$

3. Operation Principle of OSC

The general operation flowchart of the OSC is presented in Fig. 5. Embedded with the OSC, the split-core CT can alternatively operate in the correction cycle or the normal cycle. When self-correction is required, the split-core CT runs in the correction cycle. During the correction cycle, the AWL successively switches its modes according to a specific timing in Section 3.1. Based on the sampled data of $i_s^{(k)}$ and $i_a^{(1)}$, the SCA will determine the CT errors, i.e., ε and δ , as introduced in Section 3.2. After the correction cycle is accomplished, the split-core CT turns into the normal cycle. Within the normal cycle, the AWL is always off, where only i_s is sampled. Then ε and δ are utilized to correct the measurement results, i.e., A_p and φ_p .

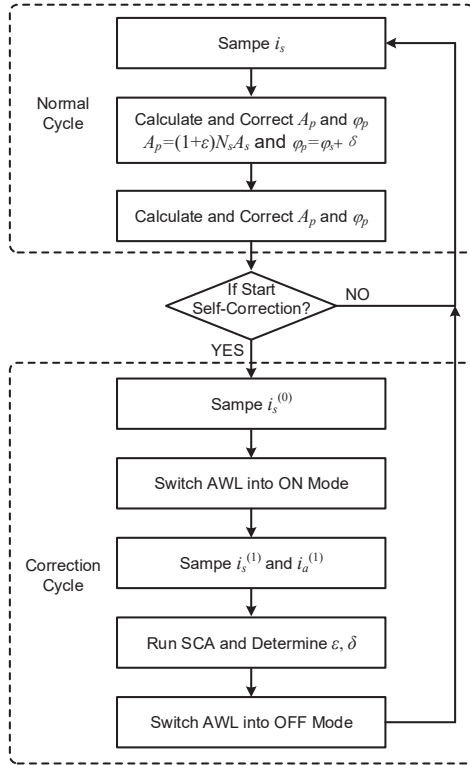


Figure 5: General operation flowchart of OSC

3.1. Mode Switching of AWL

The timing of the control signal $g(t)$ and the cycle sequence of the split-core CT are arranged as shown in Fig. 6. In detail, the mode switching of the AWL within the correction cycle is revealed in the red dashed boxes. The correction cycle is performed for a period T_c much shorter than

that of the normal cycle T_n . Wherein, the AWL successively runs under "off-on-off" mode. After mode switching, a transient process will occur, represented in the hatched area in Fig. 6. It is noticed that as the SCA depends on the steady-state current data, the sampling is only enabled over the denoted time intervals 0 and 1, when the circuit is operating in steady state. And the lengths of the above time intervals are $0.5DT_c$ ($D < 1$).

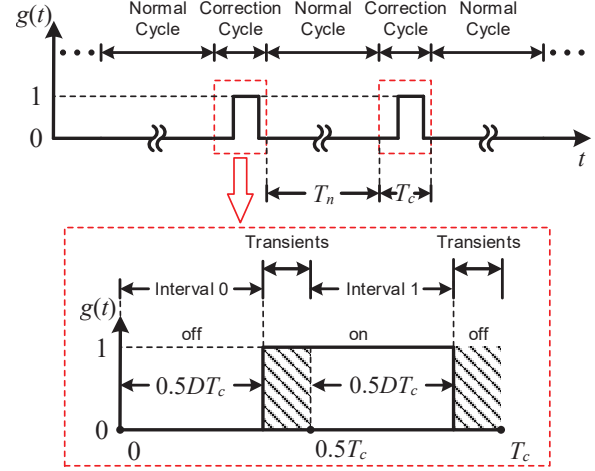


Figure 6: Cycle sequence and mode switching of AWL

3.2. Error Determination by SCA

The operation of the SCA in a correction cycle is described as Algorithm. 1.

Algorithm 1 Self-Correction Algorithm

Input:

$$f, \{i_s^{(k)}[n]\} \text{ and } \{i_a^{(k)}[n]\};$$

Output:

$$\varepsilon \text{ and } \delta;$$

- 1: Extract orthogonal components of the fundamentals of $i_s^{(k)}[n]$ and $i_a^{(k)}[n]$ based on (5);
- 2: Transform mmf-balance equation into $\mathbf{M}^{(k)}$ based on (6);
- 3: Calculate cancellation-coefficient $\mathbf{B}^{(k)}$ based on (7);
- 4: Calculate $\mathbf{B}^{(1)}\mathbf{M}^{(1)} - \mathbf{B}^{(0)}\mathbf{M}^{(0)}$ to cancel the magnetizing error components based on (8) (9), utilizing the equalities in (3) (4);
- 5: Calculate ε and δ based on (10)-(13);
- 6: **return** ε and δ

The fundamental frequency f is measured within the last normal cycle. Then time lengths $0.5DT_c$ of the intervals 0 and 1 are designed to exactly contain an integer multiple of the fundamental period $\frac{1}{2\pi f}$. Define the time of the start point of the correction cycle as $t = 0$. And the currents are sampled as: $i_s^{(k)}[n] = i_s(0.5kT_c + nT_s)$ and $i_a^{(k)}[n] = i_a(0.5kT_c + nT_s)$, where the non-negative integer $n = 0 : \frac{0.5DT_c}{T_s}$ and T_s is the sampling period of the ADCs.

Firstly, the orthogonal components of the fundamentals of $i_s^{(k)}[n]$ and $i_a^{(k)}[n]$ are extracted as:

$$\begin{aligned} \begin{bmatrix} G_s^{(k)} & H_s^{(k)} \\ G_a^{(k)} & H_a^{(k)} \end{bmatrix} &= \frac{2}{L} \sum_{n=0}^L \begin{bmatrix} i_s^{(k)}[n] \\ i_a^{(k)}[n] \end{bmatrix} \begin{bmatrix} \sin(2\pi f n T_s) \\ \cos(2\pi f n T_s) \end{bmatrix}^T \\ &= \sqrt{2} \begin{bmatrix} A_s^{(k)} \cos\varphi_s^{(k)} & A_s^{(k)} \sin\varphi_s^{(k)} \\ A_a^{(k)} \cos\varphi_a^{(k)} & A_a^{(k)} \sin\varphi_a^{(k)} \end{bmatrix} \end{aligned} \quad (5)$$

where $L = \frac{0.5DT_c}{T_s}$ is the total lengths of the sampling data $\{i_s^{(k)}[n]\}$ and $\{i_a^{(k)}[n]\}$. Then $A_s^{(k)}$ and $\varphi_s^{(k)}$ can be calculated.

On this basis, Eqn. (6) transforms mmf-balance equation, i.e. Eqn. (2), into the sums $\mathbf{M}^{(k)}$ of the orthogonal components of the fundamentals of $i_p^{(k)}[n]$ and $i_m^{(k)}[n]$. And $\mathbf{M}^{(k)}$ is calculated via $G_s^{(k)}$, $H_s^{(k)}$, $G_a^{(k)}$, and $H_a^{(k)}$ in step 2 as:

$$\begin{aligned} \mathbf{M}^{(k)} &= \frac{2}{L} \sum_{n=0}^L \begin{bmatrix} i_p^{(k)}[n] - i_m^{(k)}[n] \\ i_p^{(k)}[n] - i_m^{(k)}[n] \end{bmatrix} \begin{bmatrix} \sin(2\pi f n T_s) \\ \cos(2\pi f n T_s) \end{bmatrix}^T \\ &= \sqrt{2} \begin{bmatrix} A_p \cos\varphi_p^{(k)} - A_m \cos\varphi_m^{(k)} \\ A_p \sin\varphi_p^{(k)} - A_m \sin\varphi_m^{(k)} \end{bmatrix} = \begin{bmatrix} N_s G_s^{(k)} - N_a G_a^{(k)} \\ N_s H_s^{(k)} - N_a H_a^{(k)} \end{bmatrix} \end{aligned} \quad (6)$$

where $A_m \cos\varphi_m^{(k)}$ and $A_m \sin\varphi_m^{(k)}$ are the magnetizing error components.

Step 3 uses Eqn. (7) calculate a cancellation-coefficient $\mathbf{B}^{(k)}$ as:

$$\mathbf{B}^{(k)} = \frac{\sqrt{2}}{2} \begin{bmatrix} \frac{\cos\varphi_s^{(k)}}{A_s^{(k)}} & \frac{\sin\varphi_s^{(k)}}{A_s^{(k)}} \\ -\frac{\sin\varphi_s^{(k)}}{A_s^{(k)}} & \frac{\cos\varphi_s^{(k)}}{A_s^{(k)}} \end{bmatrix} \quad (7)$$

Then the product of $\mathbf{B}^{(k)}$ and $\mathbf{M}^{(k)}$ is constructed as:

$$\mathbf{B}^{(k)} \mathbf{M}^{(k)} = \begin{bmatrix} \frac{A_p}{A_s^{(k)}} \cos(\varphi_p^{(k)} - \varphi_s^{(k)}) - \frac{A_m}{A_s^{(k)}} \cos(\varphi_m^{(k)} - \varphi_s^{(k)}) \\ \frac{A_p}{A_s^{(k)}} \sin(\varphi_p^{(k)} - \varphi_s^{(k)}) - \frac{A_m}{A_s^{(k)}} \sin(\varphi_m^{(k)} - \varphi_s^{(k)}) \end{bmatrix} \quad (8)$$

where $\frac{A_m^{(0)}}{A_s^{(k)}} \cos(\varphi_m^{(0)} - \varphi_s^{(0)}) = \frac{A_m^{(1)}}{A_s^{(1)}} \cos(\varphi_m^{(1)} - \varphi_s^{(1)})$, and $\frac{A_m^{(0)}}{A_s^{(k)}} \sin(\varphi_m^{(0)} - \varphi_s^{(0)}) = \frac{A_m^{(1)}}{A_s^{(1)}} \sin(\varphi_m^{(1)} - \varphi_s^{(1)})$, according to Eqn. (3) (4).

Hence step 4 is to cancel these magnetizing error components via subtracting $\mathbf{B}^{(0)} \mathbf{M}^{(0)}$ from $\mathbf{B}^{(1)} \mathbf{M}^{(1)}$, while only maintaining the parts correlated to the primary current and the secondary current as:

$$\begin{aligned} \mathbf{B}^{(1)} \mathbf{M}^{(1)} - \mathbf{B}^{(0)} \mathbf{M}^{(0)} &= \begin{bmatrix} \alpha \\ \beta \end{bmatrix} \\ &= \begin{bmatrix} \frac{A_p}{A_s^{(1)}} \cos(\varphi_p^{(1)} - \varphi_s^{(1)}) - \frac{A_p}{A_s^{(0)}} \cos(\varphi_p^{(0)} - \varphi_s^{(0)}) \\ \frac{A_p}{A_s^{(1)}} \sin(\varphi_p^{(1)} - \varphi_s^{(1)}) - \frac{A_p}{A_s^{(0)}} \sin(\varphi_p^{(0)} - \varphi_s^{(0)}) \end{bmatrix} \end{aligned} \quad (9)$$

Without the effect of the magnetizing error components, the final step of the SCA calculates the real magnitude ratio N_{sr} of $i_s^{(0)}[n]$ and $i_a^{(0)}[n]$ as:

$$N_{sr} = \frac{A_p}{A_s^{(0)}} = \frac{A_s^{(1)}(\alpha^2 + \beta^2)^{\frac{1}{2}}}{(w^2 + v^2)^{\frac{1}{2}}} \quad (10)$$

where

$$\begin{cases} \theta = (\varphi_p^{(1)} - \varphi_p^{(0)}) - (\varphi_s^{(1)} - \varphi_s^{(0)}) \\ = \pi f DT_c - (\varphi_s^{(1)} - \varphi_s^{(0)}) \\ w = A_s^{(0)} \cos\theta - A_s^{(1)} \\ v = A_s^{(0)} \sin\theta \end{cases} \quad (11)$$

Therefore, ε and δ can be respectively obtained as:

$$\varepsilon = \frac{N_{sr} - N_s}{N_s} = \frac{A_s^{(1)}(\alpha^2 + \beta^2)^{\frac{1}{2}}}{N_s(w^2 + v^2)^{\frac{1}{2}}} - 1 \quad (12)$$

$$\delta = \varphi_p^{(0)} - \varphi_s^{(0)} = \arctan \frac{-v\alpha + w\beta}{w\alpha + v\beta} \quad (13)$$

3.3. Measurement Result Correction

During the next normal cycle, the magnitude A_p and phase φ_p of the primary current can be respectively corrected by ε and δ on the basis of the measured data A_s and φ_s as:

$$A_p = (1 + \varepsilon) N_s A_s \quad (14)$$

$$\varphi_p = \varphi_s + \delta \quad (15)$$

Moreover, even within the self-correction process, the primary current can keep being measured and corrected based on ε_o and δ_o determined in the last correction cycle. Thus the OSC will not interrupt the normal measurement of the split-core CT. In interval 0 of the correction cycle, A_p and φ_p can also be corrected according to (14) (15), where ε and δ are substituted by ε_o and δ_o , respectively. However, as i_a is injected within interval 1, the above equations will cause an erroneous result of the primary current. Hence additionally using $A_a^{(1)}$ and $\varphi_a^{(1)}$, the measurement results in interval 1 can be alternatively and temporarily corrected as:

$$\begin{aligned} A_p^{(1)} &= \left[(1 + \varepsilon_o)^2 N_s^2 (A_s^{(1)})^2 + N_a^2 (A_a^{(1)})^2 \right. \\ &\quad \left. - 2(1 + \varepsilon_o) N_s N_a A_s^{(1)} A_a^{(1)} \cos(\varphi_s^{(1)} - \varphi_a^{(1)}) \right]^{\frac{1}{2}} \end{aligned} \quad (16)$$

$$\varphi_p^{(1)} = \arctan \frac{(1 + \varepsilon_o) N_s A_s^{(1)} \sin\varphi_s^{(1)} - N_a A_a^{(1)} \sin\varphi_a^{(1)}}{(1 + \varepsilon_o) N_s A_s^{(1)} \cos\varphi_s^{(1)} - N_a A_a^{(1)} \cos\varphi_a^{(1)}} \quad (17)$$

4. Prototype Implementation and Experimental Tests

4.1. Design and Implementation of Prototype

The split-core CT for prototype implementation is shown in Fig. 7. This split-core CT has a rated magnitude ratio of

50 A/0.5 A/0.5 A (primary/secondary/auxiliary) and a rated 0.5 class accuracy. And the core material is silicon-steel. In fact, the real accuracy of this split-core CT is rather low, and cannot satisfy the requirement of the rated accuracy class.

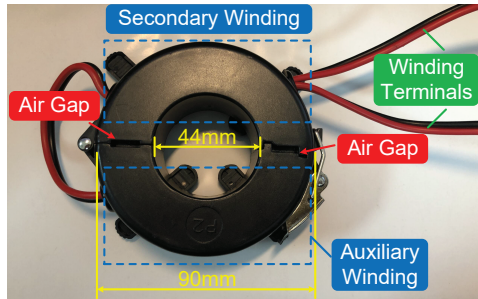


Figure 7: Split-core CT used for OSC prototype

The AWL can be implemented as shown in Fig.8, based on a three-winding isolation voltage transformer (VT in the black dashed box). The primary winding of the VT is connected to the phase line and the neutral of the low-voltage distribution networks, and the phase voltage serves as the input of the VT. One of the secondary windings of the VT with voltage u_{as} and a high-value resistor R_{as} serve as the auxiliary current source, as presented in the red dashed box. Another secondary winding and a rectifier bridge in the green dashed box are used to supply dc power for the electronic switch. Moreover, the electronic switch is designed as a solid-state relay in the blue dashed box in detail. The electronic switch is inserted into the AWL via the terminals T1 and T2. The TRIAC Q_{S2} is deployed for the switch function of the electronic switch, and is driven by the optoisolator TRIAC driver U_S . The control signal $g(t)$ of U_S is provided by the signal processor, according to the timing sequence shown in Fig. 6.

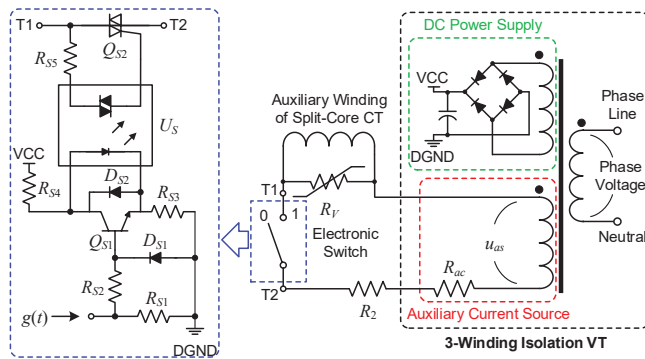


Figure 8: Implementation schematic diagram of AWL in detail

Moreover, the parameters of the selected low-cost components of the AWL and the DSP unit are listed in Table 1.

Table 1
Component parameters

Part	Component	Parameter
Shunts	R_1, R_2	0.5 or 1 Ω /2 W
	R_V	07D180K
AWL	R_{as}	20 k Ω /100 W
	R_{S1}	4.2 k Ω /0.25 W
Electronic Switch	R_{S2}	2.7 k Ω /0.25 W
	R_{S3}, R_{S4}	470 Ω /0.25 W
	R_{S5}	330 Ω /1 W
	D_{S1}, D_{S2}	1N4007
	Q_{S1}	S9013
	Q_{S2}	MAC97A8
	U_S	MOC3021
DSP Unit	ADC	AD7606
	signal processor	TMS320F28335

4.2. Setups of Experimental Test

The platform of the experimental tests is arranged with a prototype embedded with the OSC, a relay tester, standard instruments for calibration and display instruments, as shown in Fig. 9.

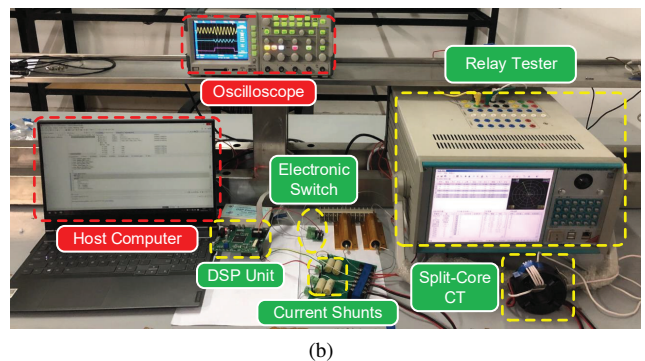
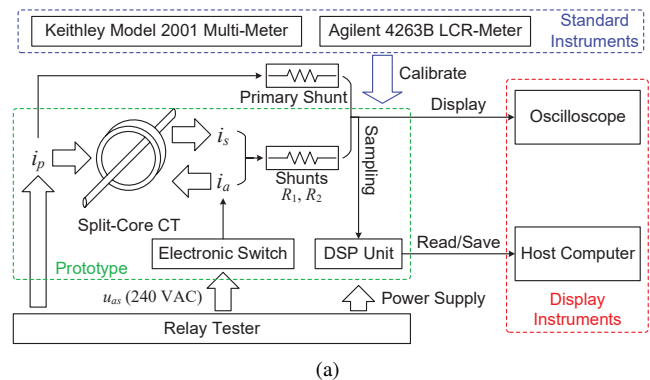


Figure 9: (a) Schematic diagram and (b) photograph of experimental test platform

The prototype contains the aforementioned split-core CT, electronic switch, DSP unit, and the shunts. The relay tester provides the primary current measured by the prototype, the

AC voltage u_{as} , and the dc power supply for the prototype. Wherein, the primary cable is distributed with the split core by 5 turns to provide an equivalent i_p with 5 times of the magnitude of the tester output current, according to the equivalent ampere-turn principle. The primary current can be sampled synchronously for reference via a shunt in series with the primary cable. u_{as} is a standard sinusoid signal with the magnitude at 240 V, and serves as the input of the AWL. The sampling rate and resolution of the DSP unit are set as 5 kS/s and 16-bit, respectively. One of the standard instruments is Keithley Model 2001 multi-meter, assigned to accurately measure the real magnitude of the primary current. And Agilent 4263B LCR-meter is used to calibrate the resistances and the slight phase displacement of the aforementioned shunts. Thus the accurate values of i_p can be obtained and used as standard references. Moreover, the oscilloscope is utilized to display the signal waveforms; and the host computer can read and save the sampled data and measurement results in tests.

4.3. Mode Switching Characteristics of AWL

When the power frequency is 50 Hz, the mode switching parameters are set as: $T_c = 0.24$ and $D = 0.667$. The waveforms of the secondary current, auxiliary winding current, and the control signal during a correction cycle are shown in Fig. 10. And the split-core CT can normally operate without unexpected issues, such as over-voltage.

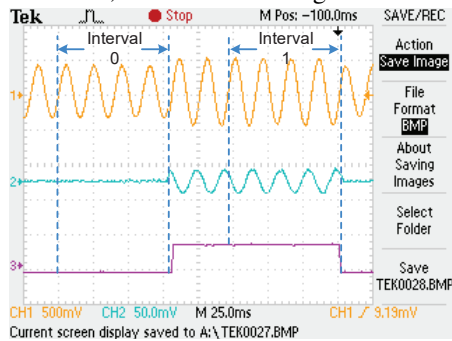


Figure 10: Secondary current (CH1), auxiliary current (CH2) and control signal (CH3) during correction cycle

Due to the nonlinearity of TRIAC in the electronic switch, the winding currents are distorted when the AWL is on in interval 1. The voltage drop on the TRIAC is shown in Fig. 11, when a standard sinusoidal signal serves as the input signal.



Figure 11: Voltage drop on TRIAC in interval 1

The spectrum of the voltage drop is presented in Fig. 12. The spectrum indicates that additional dc component and odd harmonics exist in the voltage drop of the TRIAC. Since the fundamentals of the winding currents are separately extracted based on integer-period sampling as (5), the fundamental parameters can be accurately obtained without the effect of the additional harmonics.

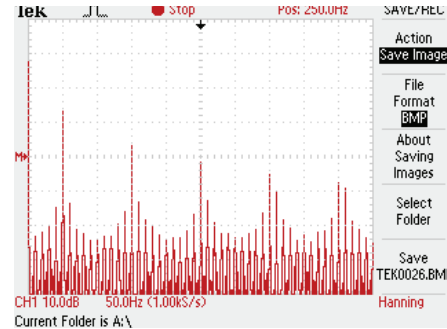


Figure 12: Spectrum of voltage drop on TRIAC

4.4. Performance of Prototype under Different Applied Primary Currents and Burdens

To comprehensively validate the performance of the OSC, 36 cases of tests have been separately taken under different applied primary currents and burdens, when the CT under test is normally installed. The setups of the applied primary currents and burdens are given in Table 2. The magnitude of the applied primary current I_p is set as 5%, 20%, 50%, 80%, 100%, or 120% of the rated value I_{pN} ($=50$ A), respectively. The magnitude of i_a in on mode is 11.6 mA. The power frequency f is adjusted as 45 Hz, 50 Hz, or 55 Hz, where the rated frequency is 50 Hz. The burden (i.e. the current shunt R_1 in Fig. 2) is configured as 1.0 Ω or 0.5 Ω precision resistor with a very low temperature coefficient. And ten repeated measurements are performed in each test case.

The error determination results of the OSC for the split-core CT are listed in Table 2. The results show the error of the split-core CT varies distinctly with values of the applied primary current magnitude (I_{pN}), the power frequency (f), and the burden R_1 . Generally, when I_{pN} increases, the absolute values of ε and δ tend to decrease. The variation of ε and δ at different I_{pN} are up to 3.8 mA/A and 8.84 mrad, respectively. The change of f has a relatively smaller effect on the variation of ε (< 2.2 mA/A), while the maximum variation of δ is 11.0 mrad. And the differences of ε and δ between the results at $R_1 = 0.5 \Omega$ and $R_1 = 1 \Omega$ are large, which can correspondingly reach 20.8 mA/A and 19.3 mrad. Taking these above into consideration, it can be known that the error of the split-core CT is significantly influenced by the applied primary current and the burden in operation.

4.4.1. Uncertainty Analysis

The determined errors depend on the current data $i_s^{(k)}[n]$ ($k=0, 1$) and $i_a^{(1)}[n]$. These data are calculated via the shunt resistances and the corresponding voltage drops. Hence the uncertainties describing the reliability of determining the errors are relevant to the uncertainty budgets contributed by the resistances, the voltages, the standard instruments, and

Table 2

Test results under operating conditions with different applied primary currents and burdens

$I_{pN} = 50 \text{ A}$		Errors and combined standard uncertainties									
		$R_1 = 1.0 \Omega$					$R_1 = 0.5 \Omega$				
$f[\text{Hz}]$	$I_p[\%]$	Case	$\varepsilon[\text{mA/A}]$	$u_{c\varepsilon}[\text{mA/A}]$	$\delta[\text{mrad}]$	$u_{c\delta}[\text{mrad}]$	Case	$\varepsilon[\text{mA/A}]$	$u_{c\varepsilon}[\text{mA/A}]$	$\delta[\text{mrad}]$	$u_{c\delta}[\text{mrad}]$
45	5	1	42.0	0.695	-13.6	0.645	19	23.4	0.839	-31.3	0.502
	20	2	39.8	0.546	-11.6	0.789	20	22.5	0.806	-30.9	0.251
	50	3	39.3	0.727	-7.63	0.597	21	21.3	0.566	-25.2	0.512
	80	4	39.0	0.603	-6.21	0.445	22	20.3	0.398	-23.9	0.730
	100	5	38.6	0.400	-5.75	0.814	23	19.4	0.769	-22.3	0.887
	120	6	38.9	0.474	-4.76	0.997	24	19.6	0.508	-22.1	0.968
50	5	7	41.9	0.502	-8.64	0.418	25	21.1	0.496	-25.6	0.407
	20	8	41.6	0.771	-7.64	0.625	26	21.2	0.401	-24.6	0.486
	50	9	39.6	0.378	-3.46	0.617	27	19.3	0.471	-19.6	0.439
	80	10	38.2	0.593	-3.00	0.709	28	19.8	0.469	-18.0	0.903
	100	11	37.7	0.530	-4.39	0.583	29	18.5	0.441	-17.8	0.964
	120	12	38.1	0.458	-1.91	0.785	30	18.5	0.489	-16.8	0.697
55	5	13	41.7	0.866	-5.71	0.780	31	21.6	0.810	-20.3	0.442
	20	14	40.7	0.247	-2.24	0.551	32	20.7	0.819	-20.4	0.461
	50	15	38.6	0.840	-1.02	0.667	33	19.6	0.715	-15.9	0.666
	80	16	38.6	0.749	-0.749	0.426	34	19.1	0.649	-14.2	0.763
	100	17	38.4	0.641	-1.14	0.956	35	18.6	0.543	-13.7	0.682
	120	18	37.9	0.487	-1.43	0.734	36	17.9	0.186	-14.5	0.487

the sampling system. For simplicity, we use the combined standard uncertainties only based on type A uncertainties of specific measurable quantities of i_s and i_a , including: $A_s^{(k)}$, $A_a^{(1)}$, $\Delta\varphi_s = \varphi_s^{(1)} - \varphi_s^{(0)}$, and $\Delta\varphi_{as}^{(k)} = \varphi_a^{(1)} - \varphi_s^{(k)}$. Based on Eqn. (12) (14), the transfer functions of the determined errors and the measurable quantities are shown as:

$$\begin{aligned} \varepsilon &= F_\varepsilon(A_s^{(0)}, \varphi_s^{(0)}, A_s^{(1)}, \varphi_s^{(1)}, A_a^{(1)}, \varphi_a^{(1)}) \\ &= \frac{N_a A_a^{(1)}}{N_s [(A_s^{(0)})^2 + (A_s^{(1)})^2 - 2A_s^{(0)} A_s^{(1)} \cos(\varphi_s^{(1)} - \varphi_s^{(0)})]^{\frac{1}{2}}} - 1 \end{aligned} \quad (18)$$

$$\begin{aligned} \delta &= F_\delta(A_s^{(0)}, \varphi_s^{(0)}, A_s^{(1)}, \varphi_s^{(1)}, A_a^{(1)}, \varphi_a^{(1)}) \\ &= \arctan \frac{A_s^{(0)} \sin(\varphi_a^{(1)} - \varphi_s^{(0)}) - A_s^{(1)} \sin(\varphi_a^{(1)} - \varphi_s^{(1)})}{A_s^{(0)} \cos(\varphi_a^{(1)} - \varphi_s^{(0)}) - A_s^{(1)} \cos(\varphi_a^{(1)} - \varphi_s^{(1)})} \end{aligned} \quad (19)$$

Define the type A uncertainties of $A_s^{(k)}$, $A_a^{(1)}$, $\Delta\varphi_s$ and $\Delta\varphi_{as}^{(k)}$ as $u_A(A_s^{(k)})$, $u_A(A_a^{(1)})$, $u_A(\Delta\varphi_s)$ and $u_A(\Delta\varphi_{as}^{(k)})$, respectively. Let $u(A_s^{(1)}, A_a^{(1)})$ be the estimated covariance of $A_s^{(1)}$ and $A_a^{(1)}$. Also, $u(A_s^{(1)}, \Delta\varphi_s)$, $u(A_a^{(1)}, \Delta\varphi_s)$, and $u(A_s^{(1)}, \Delta\varphi_{as}^{(k)})$ can be similarly defined. And these type A uncertainties and estimated covariances are obtained via the results of the repeated measurements. Then according to [24], the combined standard uncertainties of the ratio error and phase displacement, i.e. $u_c(\varepsilon)$ and $u_c(\delta)$, respectively, can be calculated as:

$$u_c(\varepsilon) = \left\{ \left[\begin{array}{c} \left(\frac{\partial F_\varepsilon}{\partial A_a^{(1)}} \right)^2 \\ \left(\frac{\partial F_\varepsilon}{\partial A_s^{(0)}} \right)^2 \\ \left(\frac{\partial F_\varepsilon}{\partial A_s^{(1)}} \right)^2 \\ \left(\frac{\partial F_\varepsilon}{\partial \Delta\varphi_s} \right)^2 \\ \frac{\partial F_\varepsilon}{\partial A_s^{(1)}} \frac{\partial F_\varepsilon}{\partial A_a^{(1)}} \\ \frac{\partial F_\varepsilon}{\partial A_a^{(1)}} \frac{\partial F_\varepsilon}{\partial \Delta\varphi_s} \end{array} \right]^T \left[\begin{array}{c} u_A^2(A_a^{(1)}) \\ u_A^2(A_s^{(0)}) \\ u_A^2(A_s^{(1)}) \\ u_A^2(\Delta\varphi_s) \\ u(A_s^{(1)}, A_a^{(1)}) \\ u(A_a^{(1)}, \Delta\varphi_s) \end{array} \right] \right\}^{\frac{1}{2}} \quad (20)$$

$$u_c(\delta) = \left\{ \left[\begin{array}{c} \left(\frac{\partial F_\delta}{\partial A_s^{(0)}} \right)^2 \\ \left(\frac{\partial F_\delta}{\partial A_s^{(1)}} \right)^2 \\ \left(\frac{\partial F_\delta}{\partial \Delta\varphi_{as}^{(0)}} \right)^2 \\ \left(\frac{\partial F_\delta}{\partial \Delta\varphi_{as}^{(1)}} \right)^2 \\ \frac{\partial F_\delta}{\partial A_s^{(1)}} \frac{\partial F_\delta}{\partial \Delta\varphi_{as}^{(0)}} \\ \frac{\partial F_\delta}{\partial A_s^{(1)}} \frac{\partial F_\delta}{\partial \Delta\varphi_{as}^{(1)}} \end{array} \right]^T \left[\begin{array}{c} u_A^2(A_s^{(0)}) \\ u_A^2(A_s^{(1)}) \\ u_A^2(\Delta\varphi_{as}^{(0)}) \\ u_A^2(\Delta\varphi_{as}^{(1)}) \\ u(A_s^{(1)}, \Delta\varphi_{as}^{(0)}) \\ u(A_s^{(1)}, \Delta\varphi_{as}^{(1)}) \end{array} \right] \right\}^{\frac{1}{2}} \quad (21)$$

The combined standard uncertainties $u_{c\varepsilon}$ and $u_{c\delta}$ are also presented in Table 2. It can be observed that the OSC determines ε and δ up to 42.0 mA/A and 31.3 mrad with $u_{c\varepsilon}$ and $u_{c\delta}$ less than 0.866 mA/A and 0.997 mrad, respectively. And in the above cases, these uncertainties are found less influenced by the changes of the operating parameters, demonstrating the reliability of error determination by the OSC.

4.4.2. Accuracy Verification

According to the arrangement in Fig. 9, i_p can also be measured by the DSP unit synchronously. And calibrated by the standard instruments, the measured values of i_p , i.e., A_p and φ_p , are used as the standard references. Compared with these standard references, the corrected measurement results in tests still have two types of measurement errors, denoted as the magnitude error λ (%) and the phase error θ (rad) as below:

$$\lambda = \left| \frac{(1 + \varepsilon)N_s A_s^{(0)} - A_p}{A_p} \right| \times 100\% \tag{22}$$

$$\theta = \left| \varphi_s^{(0)} + \delta - \varphi_p \right| \tag{23}$$

Particularly, if $\varepsilon = 0$ and $\delta = 0$ are substituted into the above equations, the inherent measurement errors of the split-core CT without the self-correction can be obtained.

The measurement errors in the tests are shown in Fig. 13 and Fig. 14, where the error limits of 0.2 class and 0.5 class at corresponding primary current prescribed by IEC 61869-2-2012 are represented as the green and purple dashed lines, respectively.

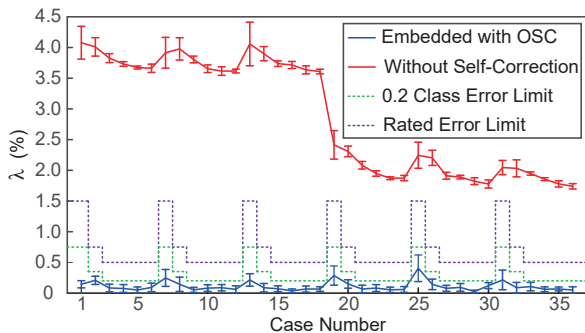


Figure 13: Magnitude errors of split-core CT

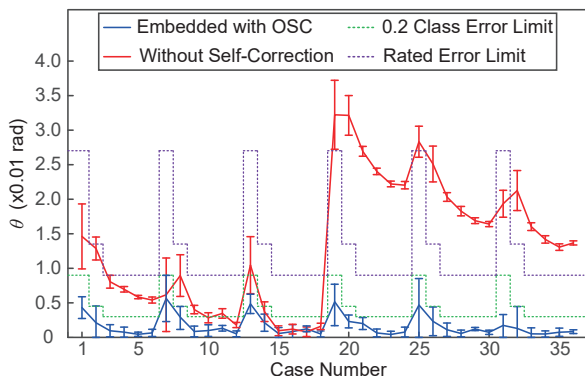


Figure 14: Phase errors of split-core CT

For comparison, the inherent measurement errors of the split-core CT without self-correction are also presented. It can be clearly observed the inherent errors substantially vary under different applied primary currents and burdens. And the inherent errors fail to meet the demand of the rated standard level (0.5). However, after being corrected by the OSC, the measurement errors are significantly reduced, and are maintained in a relatively narrow range. Then the measurement accuracy is effectively improved to a satisfactory level fully in compliance with the requirement of 0.2 class.

4.5. Performance of Prototype against Environmental Variations

4.5.1. Change of gap length

The change of the gap length by manual installation deviation and vibration is the major practical cause for the variation of the magnetizing error of split-core CTs. And this change cannot be completely avoided in long-term operation. To test the performance of the OSC against this change, the split-core CT under test is installed with an artificially configured air gap. The gap length is set from 0 (with no artificially configured air gap) to 0.520 mm with a step of 0.104 mm. In fact, the length of the gap length usually will not reach 0.520 mm in practice, while it is utilized to provide an extreme condition to test the OSC. Ten measurements are performed at each gap length. The magnitude of the applied primary current and the power frequency are 50 A and 50 Hz, correspondingly. And the burden is selected as 0.5 Ω.

The errors determined by the OSC against the gap length changes are presented in Fig. 15 and Fig. 16, respectively.

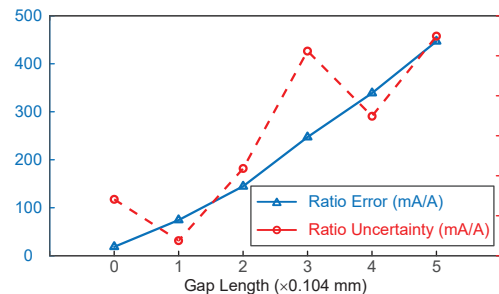


Figure 15: Ratio errors and combined standard uncertainties versus gap lengths

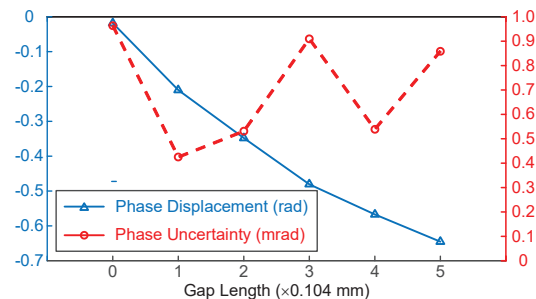


Figure 16: Phase displacements and combined standard uncertainties versus gap lengths

The results directly show that the increase of the gap length sharply degrades the performance of the split-core CT. Despite these errors varying in a wide range, the OSC

determines these errors with the combined standard uncertainties under 0.526 mA/A and 0.780 mrad, respectively.

The measurement errors of the prototype in these tests are shown in Fig. 17 and Fig. 18, respectively, in comparison with those of the split-core CT without self-correction. The results show that the increase of the gap length makes the secondary current magnitude sharply decrease to a value much smaller than the expected one, i.e., $\frac{A_p}{N_s}$; and then the measurement errors significantly increases, even resulting in total invalidity of the split-core CT. The errors of the split-core CT without self-correction correspondingly reach 30.9% and 648 mrad under the extreme condition (gap length=0.520 mm), while those without artificial air gap are 1.82% and 16.9 mrad, respectively. And when the gap length changes with 0.104 mm, the magnitude error and the phase error increase more than 5.09% and 78.7 mrad, respectively. Owing to the OSC, the measurement errors of the prototype can be effectively reduced to acceptable values below 0.195% and 0.295 mrad, respectively, which satisfies the requirements of 0.2 accuracy class. Apparently, the OSC is robust to the severe impact of the gap length change.

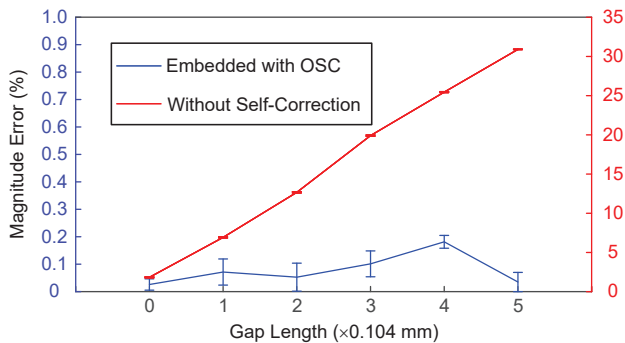


Figure 17: Magnitude errors versus gap lengths

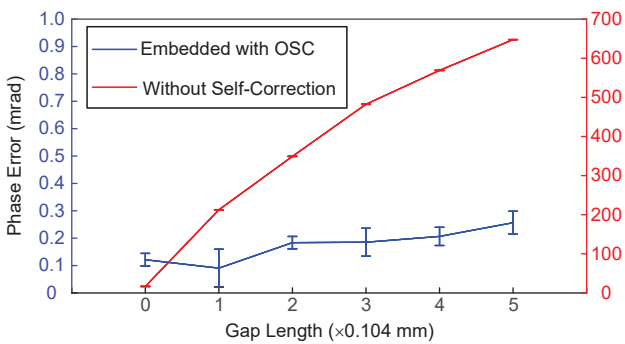


Figure 18: Phase errors versus gap lengths

4.5.2. Performance against temperature variation

The performance of the OSC against temperature variation is provided in Table 3. The CT under test works at: 1) the room temperature (25.3°C); and 2) the ambient air temperatures T heated to 36.4°C, 44.6°C and 51.1°C by a heat blower, respectively.

Table 3

Errors and combined standard uncertainties versus temperature

T (°C)	ϵ (mA/A)	u_{ce} (mA/A)	δ (mrad)	$u_{c\delta}$ (mrad)
25.3	18.5	0.441	-17.8	0.964
36.4	18.9	0.456	-19.4	0.399
44.6	20.8	0.866	-18.2	0.632
51.1	21.2	0.573	-18.0	0.418

The results show that the temperature variation leads to a relatively slight change of the ratio error and the phase displacement, not exceeding 2.30 mA/A and 1.6 mrad, respectively. And the OSC determines the errors, with combined standard uncertainties below 0.866 mA/A and 0.964 mrad, correspondingly. Notably, the magnitude errors and the phase errors of the primary current in these tests are all within 0.196% and 1.94 mrad, under the limits of 0.2 class.

5. Conclusion

This paper has proposed a online self-correction method to improve the accuracy of the split-core current transformer in low-voltage distribution networks. The proposed method includes: an auxiliary winding loop to operate in two modes, and a self-correction algorithm cooperating with the auxiliary winding loop to online determine the errors of the split-core CT for correcting the measurement results. The proposed method can improve the measurement accuracy of the split-core CT, without interrupting the measurement. Also, the proposed method can keep track of the varying errors due to the manual installation deviation and environmental variations. Moreover, this paper provides a low-cost solution for embedding the proposed method in multiple split-core CTs in low-voltage distribution network, via series-connecting auxiliary winding loops to share one set of the auxiliary current source and electronic switch.

A prototype embedded with the proposed method is implemented for validation. In experimental tests of the prototype, the proposed method reliably determines the ratio error and the phase displacement up to 42.0 mA/A and -31.3 mrad, with combined standard uncertainties below 0.866 mA/A and 0.997 mrad, respectively. Most importantly, the proposed method significantly improves the measurement accuracy to 0.2 class, while the accuracy of the CT without correction cannot satisfy the requirement of 0.5 class. Furthermore, the proposed method's robustness to the gap length change is verified. Against the error sharply increasing with the gap length, the proposed method can maintain the measurement accuracy at 0.2 class. Notably, even under the extreme condition with a 0.520 mm gap, the measurement errors are significantly reduced from the CT's inherent errors up to 30.9% and 648 mrad to a satisfactory range under 0.1% and 0.2 mrad, respectively. Also, the measurement errors below 0.196% and 1.94 mrad at different ambient temperatures confirm the proposed method's effectiveness.

References

- [1] Harlow, J.H., 2003. *Electric Power Transformer Engineering*.
- [2] Ripka, P., 2010. Electric current sensors: A review. *Measurement Science and Technology* 21, 112001.
- [3] O'Driscoll, E., O'Donnell, G.E., 2013. Industrial power and energy metering – a state-of-the-art review. *Journal of Cleaner Production* 41, 53–64.
- [4] Satthasujarit, S., Charbkaew, N., Bunyagul, T., 2015. Design of a wireless current monitoring system for distribution feeders, in: 2015 7th International Conference on Information Technology and Electrical Engineering (ICITEE), pp. 188–193.
- [5] Corney, A.C., 2001. Simple absolute method for current transformer calibration. *IEEE Transactions on Instrumentation and Measurement* 50, 278–281.
- [6] Kaczmarek, M., 2016. Measurement error of non-sinusoidal electrical power and energy caused by instrument transformers. *IET Generation Transmission & Distribution* 10, 3492–3498.
- [7] Kaczmarek, M., Stano, E., 2020. Nonlinearity of magnetic core in evaluation of current and phase errors of transformation of higher harmonics of distorted current by inductive current transformers. *IEEE Access* 8, 118885–118898.
- [8] Paudel, N., Siddharth, V., Shaw, S., Raschka, D., 2018. Electromagnetic simulation of split-core current transformer for medium voltage applications, in: COMSOL Conference.
- [9] Swieboda, C., Walak, J., Soinski, M., Rygal, J., Leszczynski, J., Grybos, D., 2019. Nanocrystalline oval cut cores for current instrument transformer prototypes. *Measurement* 136.
- [10] Houtzager, E., Rietveld, G., Dessens, J., Heemskerk, M., Brom, H.E.V.D., 2014. Design of a non-invasive current sensor for application on high voltage lines, in: CPEM 2014 (Conference on Precision Electromagnetic Measurements).
- [11] Ramboz, J.D., 1996. A highly accurate, hand-held clamp-on current transformer. *IEEE Transactions on Instrumentation and Measurement* 45, 445–448.
- [12] So, E., Bennett, D., 1997. A low-current multistage clamp-on current transformer with ratio errors below 50×10^{-6} . *IEEE Transactions on Instrumentation and Measurement* 46, 454–458.
- [13] T. M. Souders, 2004. Transformer-like devices for high-accuracy ac current measurements. NIST Technical Note 1473 .
- [14] Locci, N., Muscas, C., 2000. A digital compensation method for improving current transformer accuracy. *IEEE Transactions on Power Delivery* 15, 1104–1109.
- [15] Draxler, K., Styblíková, R., 2016. Calibration of ac clamp meters. *IEEE Transactions on Instrumentation and Measurement* 65, 1156–1162.
- [16] Siegenthaler, S., Mester, C., 2017. A computer-controlled calibrator for instrument transformer test sets. *IEEE Transactions on Instrumentation and Measurement* 66, 1184–1190.
- [17] van den Brom, H.E., Rietveld, G., So, E., 2015. Sampling current ratio measurement system for calibration of current transducers up to 10 ka with $5 \cdot 10^{-6}$ uncertainty. *IEEE Transactions on Instrumentation and Measurement* 64, 1685–1691.
- [18] Draxler, K., Styblikova, R., 2017. Calibration of instrument current transformers at low currents using lock-in amplifier, in: 2017 International Conference on Applied Electronics (AE), pp. 1–4.
- [19] Slomovitz, D., Santos, A., 2012. A self-calibrating instrument current transformer. *Measurement* 45, 2213–2217.
- [20] Aristoy, G., Santos, A., Arabadjian, H., Slomovitz, D., 2014. Burden influence on measuring transformers calibration, in: 29th Conference on Precision Electromagnetic Measurements (CPEM 2014), pp. 312–313.
- [21] So, E., Arseneau, R., Bennett, D., Frigault, M.E., 2011. A current-comparator-based system for calibrating high-voltage current transformers under actual operating conditions. *IEEE Transactions on Instrumentation and Measurement* 60, 2449–2454.
- [22] Jung, J.K., So, E., Park, Y.T., Kim, M., 2009. Kriss-nrc intercomparisons of calibration systems for instrument transformers with many different ratios at power frequency. *IEEE Transactions on Instrumentation and Measurement* 58, 1023–1028.
- [23] Djokić, B.V., Parks, H., Wise, N., Naumović-Vuković, D., Škundrić, S.P., Žigić, A.D., Polužanski, V., 2017. A comparison of two current transformer calibration systems at nrc canada. *IEEE Transactions on Instrumentation and Measurement* 66, 1628–1635.
- [24] Salicone, S., 2006. *Measurement Uncertainty: An Approach Via the Mathematical Theory of Evidence*.